RSC Advances

ROYAL SOCIETY OF CHEMISTRY

PAPER

View Article Online
View Journal | View Issue

Check for updates

Cite this: *RSC Adv.*, 2024, **14**, 7157

Atomically dispersed nanozyme-based synergistic mild photothermal/nanocatalytic therapy for eradicating multidrug-resistant bacteria and accelerating infected wound healing†

Ying Qu,[a] Liang Zhuang,[b] Wuren Bao,[a] Chunlin Li,[c] Hongyu Chen,[d] Shan He,*[b] Hui Yao*[d] and Quanjin Si*[c]

Received 10th December 2023
Accepted 15th February 2024

DOI: 10.1039/d3ra08431k

rsc.li/rsc-advances

Constructing a synergistic multiple-modal antibacterial platform for multi-drug-resistant (MDR) bacterial eradication and effective treatment of infected wounds remains an important and challenging goal. Herein, we developed a multifunctional Cu/Mn dual single-atom nanozyme (Cu/Mn-DSAzymes)-based synergistic mild photothermal/nanocatalytic-therapy for a MDR bacterium-infected wound. Cu/Mn-DSAzymes with collaborative effects exhibit remarkable dual CAT-like and OXD-like enzyme activities and could efficiently catalyze cascade enzymatic reactions with a low level of H_2O_2 as an initial reactant to produce reparative O_2 and lethal $^{\bullet}O_2^-$. Moreover, a black N-doped carbon nanosheet supports of Cu/Mn-DSAzymes show superior NIR-II-triggered photothermal performance, endowing them with photothermal-enhanced dual enzyme catalysis. In addition, such enhanced dual enzyme catalysis likely improves the susceptibility and lethality of photothermal effects on MDR bacteria. *In vitro* and *in vivo* studies demonstrate that Cu/Mn-DSAzyme-mediated synergistic nanocatalytic and photothermal effects possess dramatic antibacterial outcomes against MDR bacteria and evidently reduced inflammation at wound sites. Moreover, the combined photothermal effect and O_2 release mediated by Cu/Mn-DSAzymes promotes macrophage polarization to reparative M2 phenotype, collagen deposition, and angiogenesis, considerably accelerating wound healing. Therefore, Cu/Mn-DSAzyme-based synergetic dual-modal antibacterial therapy is a promising strategy for MDR bacterium-infected wound treatment, owing to their excellent antibacterial ability and significant tissue remodeling effects.

1 Introduction

Bacterial infections are currently considered one of the most challenging issues, posing a huge threat to public health.[1–3] More importantly, the abuse of antibiotics has led to the emergence of a large number of multi-drug-resistant (MDR) bacteria, which cause almost one million deaths each year worldwide.[3–5] To address this serious issue, numerous chemically engineered functional nanoagents with strong antibacterial effects have emerged as potential substitutes for traditional antibiotics.[3,6–9] Among them, nanozymes, a class of nanocatalytic agents with enzyme-like characteristics, represent a new development direction for MDR bacterial infection treatment.[3,6,10–12] In particular, nanozyme-based nanocatalytic antibacterial therapy has sparked increasing interest as it does not readily result in drug resistance and shows prospective antibacterial effects.[3,6,10–12] Specifically, nanozymes can mimic oxidoreductases (such as peroxidase (POD), oxidase (OXD), and catalase (CAT)) to boost local cytotoxic reactive oxygen species (ROS) and reparative O_2 levels at wound sites, thereby effectively killing MDR bacteria and significantly promoting wound healing.[6,10–15] However, nanozyme-based nanocatalytic therapy shows limited antibacterial efficiency, resulting from the inherent inefficiency of monotherapy and unsatisfactory nanozyme catalytic activity. Thus, the integration of nanozyme-based nanocatalytic therapy with other therapeutic modalities and the development of more efficient nanozymes are highly desired.

Mild photothermal therapy (M-PTT), which depends on photothermal nanoagents to generate cytotoxic heat (lower than 50 °C) under near-infrared (NIR) laser irradiation, is a promising nonresistant therapeutic modality for destroying MDR

---

[a] College of Nursing, Inner Mongolia Minzu University, Tongliao, Inner Mongolia, 028000, China

[b] Key Laboratory of Geriatric Nutrition and Health, Ministry of Education, Beijing Technology and Business University, 11 Fucheng Road, Haidian District, Beijing, 100048, P. R. China. E-mail: vh30@163.com

[c] The Third Healthcare Department of the 2nd Medical Center, Chinese PLA General Hospital, Beiing 100853, China. E-mail: quanjin2004@sohu.com

[d] Pain Department, Eye Hospital China Academy of Chinese Medical Sciences, Beijing, 100040, China. E-mail: foxyaohui@126.com

† Electronic supplementary information (ESI) available. See DOI: https://doi.org/10.1039/d3ra08431k

bacteria and preventing normal tissues from destruction by excessive temperature.[16–19] Notably, heat from M-PTT can cause significant damage to MDR bacteria. Furthermore, it can promote ROS generation by accelerating oxidoreductase-like catalysis and increase ROS permeability into bacterial membranes by inactivating the bacterial extracellular matrix, thus enabling synergistically enhanced antibacterial efficiency.[6,9,20] Moreover, M-PTT was beneficial for collagen synthesis, angiogenesis and accelerated blood circulation, thereby facilitating bacterium-infected wound healing.[9,16,21] However, the mild photothermal antibacterial effect is far from sufficient owing to the up-regulated expression of heat shock proteins (HSPs), which repair thermally damaged bacteria and cause the thermotolerance of bacteria upon laser irradiation.[16,22–24] Encouragingly, ROS can effectively destroy the activity of HSPs, since ROS can crosslink the primary amines of proteins to destroy their structure and function.[16,25,26]

Meanwhile, ROS can disrupt the bacterial membrane to make it more susceptible to M-PTT.[16,25,26] Thus, the production of plentiful ROS would be beneficial for improving the antibacterial efficiency of mild PTT. As a result, developing a nanozyme-based synergistic mild photothermal/nanocatalytic therapy would provide a versatile strategy to effectively combat MDR bacteria and accelerate wound healing. However, a crucial challenge is how to reasonably design multifunctional nanoenzymes with satisfactory enzyme activity and photothermal conversion efficiency, while exquisitely integrating synergistic dual-mode therapy into a single therapeutic nanoplatform, so as to simultaneously enhance anti-infection and tissue remodeling effects.

Recently, single-atom nanozymes (SAzymes), as a new type of mimicry enzyme, have been ingeniously developed and exhibited great potential in biomedical applications due to their maximum atom-utilization efficiency, unique enzyme-like characteristics, and multifunctionalities.[25–28] Typically, SAzymes consist of isolated active metal atoms anchored on nitrogen-doped carbon matrices, thereby giving atomically-dispersed catalytic active centers.[25–28] Moreover, SAzymes can offer porous N-doped nanocarbon matrices with a near-infrared response.[25–28] Herein, we first developed a multifunctional dual single-atom nanozyme composed of Cu and Mn (Cu/Mn-DSAzymes). Taking the Cu/Mn-DSAzymes as a model, we further constructed a synergistic mild photothermal/nanocatalytic therapy for the MDR bacteria-infected wound (Scheme 1). Cu/Mn-DSAzymes with collaborative effects were found to have remarkable dual CAT-like and OXD-like enzyme activities, and could efficiently catalyze the cascade enzymatic reactions with a low level of H_2O_2 as the initial reactant to produce abundant reparative O_2 and lethal $^{\bullet}O_2^-$. Moreover, the black N-doped carbon nanosheet supports of Cu/Mn-DSAzymes exhibited superior NIR-II-triggered photothermal performance, endowing them with photothermal-enhanced dual enzyme catalysis. In addition, such enhanced dual enzyme catalysis likely improved the susceptibility and lethality of photothermal effects on MDR bacteria. *In vitro* and *in vivo* studies demonstrated that the Cu/Mn-DSAzymes-mediated synergistic nanocatalytic and photothermal effects possessed dramatic antibacterial outcomes against MDR bacteria, and obviously reduced the inflammation at the wound sites. Moreover, the combined photothermal effect and O_2 release mediated by the Cu/Mn-DSAzymes promoted the macrophage polarization to reparative M2 phenotype, collagen deposition, angiogenesis, considerably accelerating tissue regeneration and wound healing. Therefore, Cu/Mn-DSAzyme-based synergetic mild photothermal/nanocatalytic therapy is a promising strategy for MDR bacteria-infected wounds treatment, owing to its excellent antibacterial ability and significant tissue remodeling effects.

2 Experimental section

2.1 Preparation of Cu/Mn-DSAzymes

The Cu/Mn-BTC MOF precursor was initially synthesized through a chemical precipitation method. In a succinct procedure, a mixture of $Cu(CH_3COO)_2 \cdot H_2O$ (0.162 g) and $Mn(CH_3COO)_2 \cdot 4H_2O$ (0.058 g) was dissolved in a 100 mL ethanol–water solution. Subsequently, 0.116 g of 1,3,5-benzenetricarboxylic acid was dissolved in another 100 mL ethanol–water solution and added to the above mixture, which was stirred at room temperature for 2 hours. The resulting solid products were separated through centrifugation, thoroughly washed with water, and subsequently dried in a vacuum oven.

Subsequently, 0.1 g of the Cu/Mn-BTC MOF precursor was meticulously blended with dicyandiamide through grinding until a homogeneous mixture was achieved. The resultant blend underwent heating in a tube furnace at 800 °C under N_2 flow for 3 hours. Following pyrolysis, the resulting products were washed extensively with ethanol/deionized water and dilute acid under ultrasound, culminating in the synthesis of the final Cu/Mn-DSAzymes.

2.2 Photothermal effect and photothermal conversion efficiency

The Cu/Mn-DSAzymes solution with various concentrations (0, 40, 80, and 160 $\mu g\ mL^{-1}$) was exposed to 1064 nm laser (1.0 W cm^{-2}) for 10 min, and the temperature variation was monitored by a thermocouple probe to an accuracy of 0.1 °C. The photothermal effect of the Cu/Mn-DSAzymes solution (80 $\mu g\ mL^{-1}$) under irradiation from various laser power densities (0.6, 1.0 and 1.4 W cm^{-2} of 1064 nm laser) was measured in the same way.

The photothermal conversion efficiency (η) was calculated using the following equation (eqn (1)).

$$\eta = \frac{hs(T_{\max} - T_{\text{amb}}) - Q^0}{I\left(1 - 10^{-A\lambda}\right)} \tag{1}$$

where h was the heat transfer coefficient, s was the surface area of the container, $T_{\max} - T_{\text{amb}}$ was the temperature change of the solution under continuous irradiation by a 1064 nm laser, Q^0 was the heat input due to light absorption by the solvent, I was the laser density (1.0 W cm^{-2}) and $A\lambda$ was the absorbance at 1064 nm. The value of hs can be calculated using the following equation (eqn (2)).

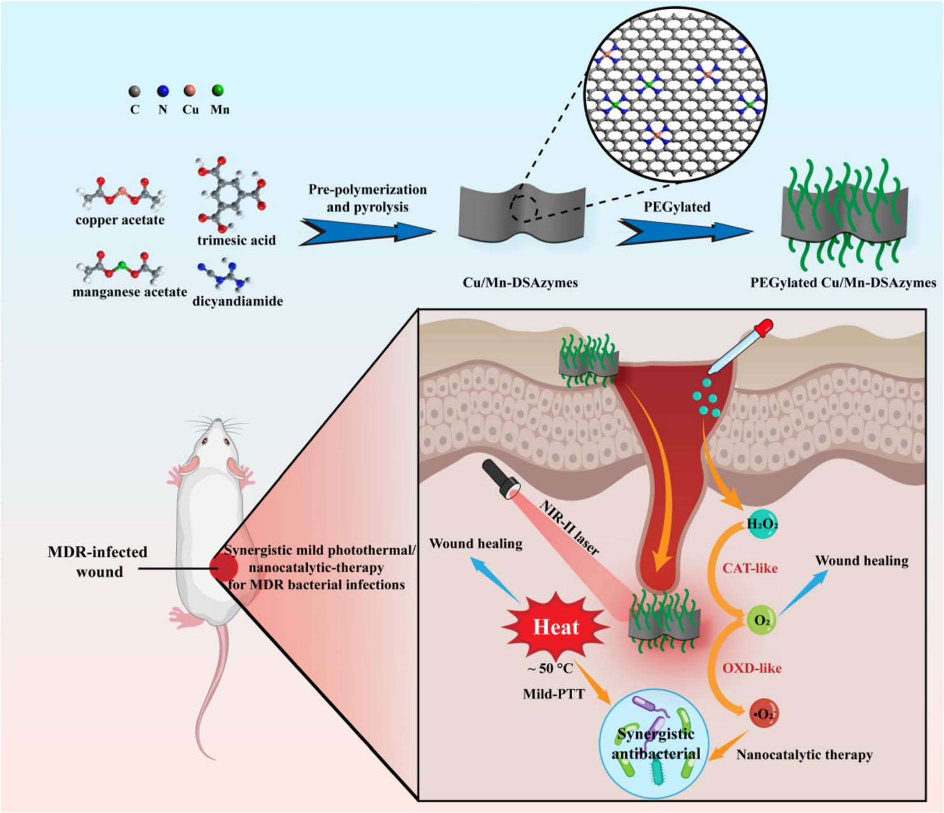

Scheme 1 Schematic illustration of the main mode of action for the Cu/Mn-DSAzyme-based synergetic mild photothermal/nanocatalytic therapy for MDR bacterium-infected wounds.

$$hs = \frac{m_D \times C_D}{\tau_s} \tag{2}$$

where m_D (1.0 g) and C_D (4.2 J g^{-1}) were the mass and heat capacity, respectively, of the deionized water dispersion medium. τ_s represented the rate of heat transfer from the solution to the environment, which was calculated using the equation (eqn (3)).

$$\tau_s = -\frac{t}{\ln \theta} \tag{3}$$

The value of τ_s was gained by the linear relationship between $-\ln(\theta)$ and time (t) obtained from the cooling period of the Cu/Mn-DSAzymes.

2.3 Measurement of CAT-like activity

The CAT-like activity of Cu/Mn-DSAzymes was assessed by quantifying the oxygen production using a portable dissolved oxygen meter. Specifically, Cu/Mn-DSAzymes at a concentration of 80 μg mL^{-1} was combined with varying concentrations of H_2O_2 (1, 2, and 4 mM) in a PBS solution. Subsequently, the real-time oxygen concentration was recorded over a 10 minutes duration.

Furthermore, kinetic assays of Cu/Mn-DSAzymes with H_2O_2 as the substrate were conducted by introducing different concentrations of H_2O_2 solution. For each H_2O_2 concentration, the initial reaction rates (V_0) were determined based on changes in the real-time oxygen concentration. The resulting rates were graphed against H_2O_2 content and subjected to fitting with Michaelis–Menten curves (eqn (4)). This fitting facilitated the determination of the Michaelis–Menten constant (K_m) and maximal reaction velocity (V_{max}), where [S] represented the substrate content.

$$v_0 = \frac{V_{\max} \cdot [S]}{K_m + [S]} \tag{4}$$

2.4 Measurement of OXD-like activity

DPBF was employed to ascertain the presence of superoxide radicals ($^{\bullet}O_2^{-}$). Specifically, a solution containing Cu/Mn-DSAzymes (80 μg mL^{-1}), H_2O_2 (1 mM), and DPBF was introduced into a PBS solution. The production of $^{\bullet}O_2^{-}$ was quantified by monitoring the reduction in absorbance at 420 nm.

OXD-like kinetic assays of Cu/Mn-DSAzymes with TMB as the substrate were conducted by introducing varying concentrations of TMB solution. For each TMB concentration, the initial reaction rates (V_0) were determined based on absorbance changes using the Beer–Lambert law (eqn (5)). Subsequently, the rates were graphed against the TMB content and subjected to fitting with Michaelis–Menten curves (eqn (4)). Utilizing the Michaelis–Menten model (eqn (4)) facilitated the determination of the Michaelis–Menten constant (K_m) and maximal reaction velocity (V_{max}).

$$A = \varepsilon bc \tag{5}$$

2.5 *In vitro* antibacterial activity

The antibacterial efficacy of Cu/Mn-DSAzymes was evaluated using the agar plate dilution method and the growth curve method. In the agar plate dilution approach, MRSA and *E. coli* bacteria were cultured in lysogeny broth medium at 37 °C for 16 hours to attain the logarithmic growth phase. Subsequently, the bacterial solution was treated with PBS + H_2O_2 (0.1 mM), NIR-II + H_2O_2 (0.1 mM), Cu/Mn-DSAzymes, Cu/Mn-DSAzymes + NIR-II, Cu/Mn-DSAzymes + H_2O_2 (0.1 mM), and Cu/Mn-DSAzymes + H_2O_2 (0.1 mM) + NIR-II groups at 37 °C for 4 hours, maintaining an equivalent Cu/Mn-DSAzyme concentration of 80 μg mL^{-1}. In cases involving NIR-II irradiation, the samples were exposed to a 1064 nm laser. The resulting bacterial suspensions were diluted 10 000 times, and 50 μL of the diluted solution was plated onto solid culture medium. These Petri dishes were then incubated at 37 °C for 24 hours to observe bacterial growth. The colony-forming units (CFU) of MRSA and *E. coli* were subsequently enumerated. For the growth curve method, suspensions of MRSA and *E. coli* treated with various groups were mixed in LB medium. These different treatment groups were then added to 96-well plates ($n = 3$), and incubated in a fully automated growth curve analyzer (Bioscreen C). The optical density values were monitored at a wavelength of 600 nm (OD600) until the growth curve reached a plateau stage.

SYTO9 and PI double staining was employed to discern live/dead MRSA and *E. coli* bacteria following diverse treatments. Fluorescent images were captured using confocal laser scanning microscopy. For reactive oxygen species (ROS) detection, DCFH-DA was utilized to label MRSA bacteria under distinct treatments, and the fluorescence intensity of DCF reflected the ROS levels. To investigate the bacterial morphology, MRSA and *E. coli* bacteria subjected to various treatments were fixed with 2.5% glutaraldehyde for 2 hours at room temperature. Subsequently, the bacteria underwent sequential treatment with ethanol concentrations of 50%, 70%, 80%, 90%, 95%, and 100%. The resulting bacterial morphology was observed using scanning electron microscopy (SEM).

2.6 *In vitro* antibacterial mechanism

The antibacterial mechanism was elucidated through the assessment of K^+, β-galactosidase, and DNA leakage from MRSA. K^+ levels were measured by incubating MRSA in LB medium at 37 °C for 24 hours, followed by treatment with various groups and subsequent analysis of MRSA suspensions. The concentration of K^+ was determined using sodium tetraphenylboronate. To assess the β-galactosidase activity, MRSA was cultured in LB medium at 37 °C for 24 hours. The collected bacteria were subsequently incubated in M9 lactose medium at 37 °C for 8 hours, followed by centrifugation and collection. Bacterial suspensions were mixed with different treatment groups and incubated at 37 °C. The supernatant was collected at different intervals, and the optical density of *p*-nitrophenol was measured at 400 nm using a microplate reader. Concentrations of K^+ and β-galactosidase were calculated based on standard curves. Intra-bacterial DNA levels were determined by measuring the OD260 values of the supernatant of bacterial suspensions after diverse treatments. Briefly, MRSA was treated with different groups and incubated at 37 °C. Subsequently, bacterial suspensions were centrifuged, and the absorbance value of the resulting supernatants was read at 260 nm.

2.7 Cytotoxicity evaluation

The biocompatibility assay of Cu/Mn-DSAzymes was conducted on L929 cells using a Cell Counting-Kit 8 (CCK-8) assay. Initially, cells were incubated in a 25 cm^2 cell-culture flask and subsequently seeded into a 96-well plate (1×10^4 cells per well) by pipetting. The cell medium was then replaced with fresh medium containing different concentrations of Cu/Mn-DSAzymes (0, 20, 40, 80, and 160 μg mL^{-1}). Following a 24 hours incubation, the cells were washed once with PBS and further incubated with CCK-8 for 1 hour. Moreover, after co-incubation with Cu/Mn-DSAzymes (80 μg mL^{-1}) for 24 hours, 72 hours, and 120 hours, respectively, the L929 cells were double stained with calcein-AM and PI to distinguish live/dead cells. Fluorescent images were obtained using confocal laser scanning microscopy. For the hemocompatibility assay, fresh red blood cells (RBCs) were obtained from mice and diluted with normal saline. The RBC suspensions were then co-incubated with normal saline (negative control), distilled water (positive control), or different concentrations of Cu/Mn-DSAzymes. The supernatant was subsequently removed by centrifugation, the absorbance was measured at 545 nm, and the hemolysis rate was calculated.

2.8 *In vivo* healing of MRSA-infected wounds

All animal experiments strictly adhered to the relevant laws and institutional guidelines of the University of Chinese Academy of Sciences (UCAS), and received approval from the Model Animal Research Center of the Institute of Process Engineering, Chinese Academy of Sciences. Dorsal hair of ICR mice (6 weeks old, female) was shaved, and full-thickness defective skin wounds were created. Following wound formation, the MRSA suspension was inoculated at the wound sites. To confirm the success of infection, bacterial samples were collected from the wounds *via* sterilized cotton swabs at 12 hours post-infection or 9 days post-management. Swabs were placed in 1 mL of normal saline solution, and loads of live MRSA in diluted suspensions were investigated after culturing MRSA on LB agar plates for 24 hours at 37 °C. MRSA-infected ICR mice were randomly divided into five groups ($n = 5$) and treated with PBS + H_2O_2 (0.1 mM), NIR-II + H_2O_2 (0.1 mM), Cu/Mn-DSAzymes, Cu/Mn-DSAzymes + NIR-II, Cu/Mn-DSAzymes + H_2O_2 (0.1 mM), and Cu/Mn-DSAzymes + H_2O_2 (0.1 mM) + NIR-II groups, respectively. The irradiation group was exposed to a 1064 nm laser. On days 0, 3, 5, 7, and 9, the wound sites were measured to calculate the degree of wound healing. The body weights of mice were recorded for 9 days. On day 9, the wound and surrounding tissues were harvested, fixed with a 10% formaldehyde solution, dehydrated, embedded in paraffin, and sectioned for H&E or Masson's trichrome staining, revealing histopathological characteristics of the wounds treated with different groups. Wound tissues treated with different groups were collected on day 9, and the immunofluorescent staining of CD86, CD206, and CD31 was analyzed.

2.9 Statistical analysis

Statistical significance was evaluated utilizing a one-way ANOVA analysis on SPSS 16.0 software. Differences were considered statistically significant if the probability value was less than 0.05 ($p < 0.05$). Mean values and standard deviations (SD) were computed for triplicate experiments. All data are expressed as mean ± SD.

3. Results and discussion

3.1. Synthesis and structural characterization of Cu/Mn-DSAzymes

Initially, N-doped carbon nanosheets-supported Cu/Mn dual single-atom nanozymes (Cu/Mn-DSAzymes) were synthesized *via* a facile two-step approach (see the Experimental section for details). Briefly, diatomic Cu/Mn-BTC MOF precursors (with a typical crystalline structure and rod-shaped morphology of BTC MOFs, as shown in Fig. S1†) were prepared by mixing copper acetate and manganese acetate with trimesic acid, followed by a chemical precipitation process. In particular, the obtained Cu/Mn-BTC MOF precursors consisted of structural primitives of binuclear metal complexes containing oxygen donor ligands, which could provide ordered and periodic bimetal nodes with binuclear homologous and binuclear heterogeneous Cu/Mn atoms. Afterwards, the precursors were mixed with dicyandiamide as a nitrogen source, followed by pyrolysis at 800 °C under a nitrogen atmosphere. During the heat-treatment process, Cu/Mn-BTC MOF precursors containing the carboxylic acid groups of the trimesic acid could react with dicyandiamide, giving rise to ultrathin 2D N-doped carbon nanosheet matrices. At the same time, Cu and Mn species can be securely trapped by the N-rich porous carbon and *in situ* anchored onto the formed nitrogenated carbon nanosheets. After complete annealing, the resulting products were washed by deionized water and dilute acid under ultrasound, obtaining Cu/Mn-DSAzymes. In addition, N-doped carbon nanosheets (CNNs) were prepared as control samples. Transmission electron microscopy (TEM) images revealed that the Cu/Mn-DSAzymes had a nanometer-sized 2D nanosheet structure (Fig. 1a). Moreover, the hydrodynamic size and zeta potential ζ of the Cu/Mn-DSAzymes was measured to be ∼132 nm and ∼26.9 mV, respectively (Fig. 1b), which implied their good stability and dispersibility in the physiological medium. Powder X-ray diffraction (XRD) analysis of Cu/Mn-DSAzymes is presented in Fig. 1c. The as-prepared Cu/Mn-DSAzymes exhibited a relatively strong peak at ∼26.4° and one weak peak at ∼44.5°, respectively, corresponding to the (002) and (101) diffraction planes of the graphite-2H phase (PDF 41-1487). This indicated that neither oxide nor metal nanoparticles existed in Cu/Mn-DSAzymes. Next, aberration-corrected high-angle annular dark-field scanning transmission electron microscopy (AC-HAADF-STEM) was utilized to investigate the local distribution of Cu and Mn atoms. The AC-HAADF-STEM images of Cu/Mn-DSAzymes (Fig. 1d and e) showed that a dense distribution of the single atoms (highlighted by dashed yellow circles) was homogeneously anchored on the N-doped carbon nanosheets. Inductively coupled plasma atomic emission spectroscopy (ICP-AES) analysis verified that Cu/Mn-DSAzymes possessed a metal atom loading of 4.9 wt% (3.2 wt% of Cu and 1.7 wt% of Mn). Moreover, energy-dispersive X-ray spectroscopy (EDS) elemental mapping revealed the homogeneous distribution of C, N, Cu and Mn over the entire nanosheet (Fig. 1f). Therefore, these data confirmed the formation of Cu/Mn dual single-atom sites.

To further confirm the coordination structure of the Cu/Mn elements at the atomic level, X-ray absorption spectroscopy (XAS) analysis of Cu/Mn-DSAzymes, as well as referenced Cu foil, CuO, Mn foil, and MnO_2 was employed. First, the Cu K-edge Fourier-Transformed (FT) k^3-weighted extended X-ray absorption fine structure (EXAFS) spectra of Cu/Mn-DSAzymes displayed the main peak at ∼1.48 Å in R-space, which can be attributed to the coordination of Cu–N (Fig. 1g). Meanwhile, the Mn K-edge FT-EXAFS spectra showed a main peak at ∼1.63 Å, belonging to Mn–N coordination (Fig. 1h). In addition, no obvious metallic Cu–Cu or Mn–Mn coordination was found, suggesting that all metal in Cu/Mn-DSAzymes was atomically dispersed on the N-doped carbon nanosheets. Furthermore, to reveal the electronic structures of Cu/Mn-DSAzymes, high-resolution X-ray photoelectron spectroscopy (XPS) was performed. The N 1s spectra (Fig. 1i) can be deconvoluted into four peaks at binding energies of 398.3, 399.0, 400.5, and 401.1, assigned to pyridinic N, Cu/Mn–N, pyrrolic N, and graphitic N, respectively.[29] The C 1s spectra (Fig. 1j) were deconvoluted into three peaks at 284.5, 285.4, and 287.2 eV, belonging to C–C, C–N, and C–O environments, respectively.[30] These results further verified that the Cu/Mn dual single-atom sites were atomically dispersed and anchored on the 2D nitrogenated carbon nanosheets. Next, the Cu 2p spectra (Fig. 1k) confirmed that Cu^+ (around 932.5 eV) was the dominant copper species in Cu/Mn-DSAzymes.[31] Thus, it was implied that Cu/Mn-DSAzymes could provide the Cu^+ sites for the OXD-mimicking decomposition of H_2O_2. Moreover, the Mn 2p spectra (Fig. 1l) indicated that Mn^{4+} (around 642.1 eV) existed in Cu/Mn-DSAzymes as the dominant Mn species.[32] This result suggested that Cu/Mn-DSAzymes possessed potential CAT-like activities.

3.2. Photothermal and nanocatalytic performance of Cu/Mn-DSAzymes

Compared with the NIR-I region, the NIR-II region has recently attracted widespread attention in the biomedical field, owing to its deeper tissue penetration and lower light scattering.[33] Cu/Mn-DSAzymes absorbed strongly from the visible to the NIR-II region (Fig. 2a), which endowed them with good potential as

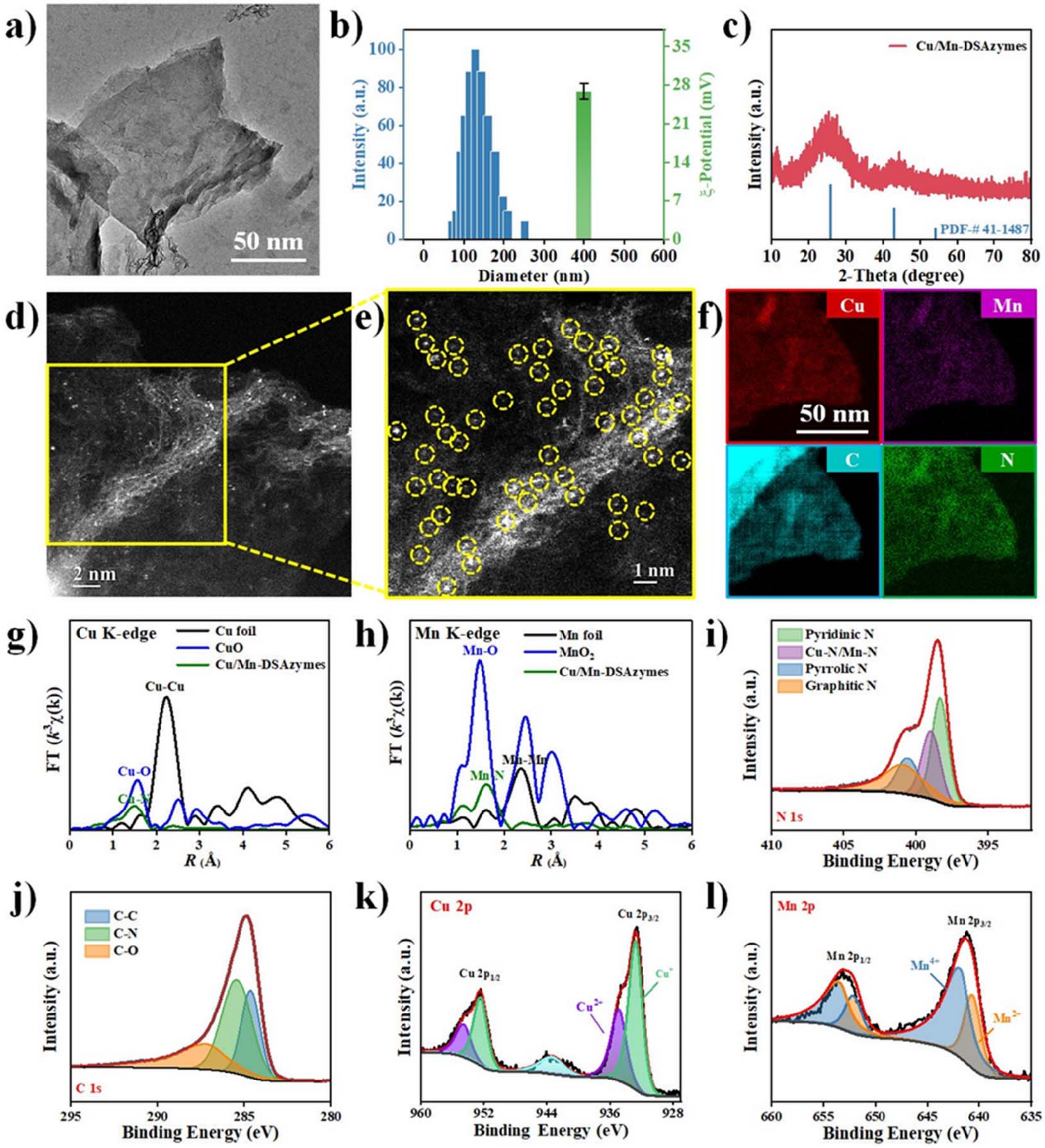

Fig. 1 (a) TEM image of Cu/Mn-DSAzymes. (b) The size distribution and zeta potential ζ of Cu/Mn-DSAzymes. (c) XRD patterns of Cu/Mn-DSAzymes. (d) AC-HAADF-STEM images of Cu/Mn-DSAzymes. (e) Magnified AC-HAADF-STEM image of the yellow-frame area in (d). (f) EDS mapping patterns for Cu, Mn, C and N elements of Cu/Mn-DSAzymes. (g) Cu and (h) Mn K-edge Fourier-transform k^3-weighted EXAFS spectra of Cu/Mn-DSAzymes. (i) N 1s and (j) C 1s XPS spectra. (k) XPS Cu 2p spectra and (l) Mn 2p spectra of Cu/Mn-DSAzymes.

NIR-II-triggered photothermal agents for wound treatment. Here, the NIR-II-triggered photothermal performance of Cu/Mn-DSAzymes was evaluated by detecting their temperature variation under 1064 nm laser irradiation for 10 min. The PBS (Fig. 2b) showed a very small temperature variation, and only rose from 25.2 to 28.3 °C. By contrast, the photothermal performance of Cu/Mn-DSAzymes and the irradiation power (Fig. 2c) were significantly dependent on the concentration (Fig. 2b) as the concentration changed to 40, 80, and 160 μg mL^{-1} respectively, the temperature can correspondingly increase to 35.6 °C, 49.0 °C, and 58.3 °C. When the laser power density was adjusted to 0.6 W cm^{-2}, 1.0 W cm^{-2}, the temperature can also correspondingly rise to 40.2 °C, 48.8 °C, and 59.6 °C, and 1.4 W cm^{-2} respectively. Moreover, the photothermal conversion efficiency (η) of Cu/Mn-DSAzymes was calculated to be 38.7% from the heating and cooling curves (see Fig. 2d and the ESI† for details). In addition, Cu/Mn-DSAzymes (Fig. 2e) showed no obvious temperature drop after five alternating heating and cooling cycles, suggesting a very stable photothermal effect. Therefore, the Cu/Mn-DSAzymes could be used as an excellent photothermal agent for NIR-II triggered photothermal therapy of bacteria-infected wounds.

Furthermore, the dual enzyme-like properties and nanocatalytic performance of Cu/Mn-DSAzymes were investigated in detail, wherein the CAT-like enzyme catalyzed the decomposition of H_2O_2 to O_2, and the OXD-like enzyme catalyzed the conversion of O_2 into $^{\bullet}O_2^-$. As shown in Fig. 2f, the Cu/Mn-DSAzymes possessed significant oxygen production capacity in

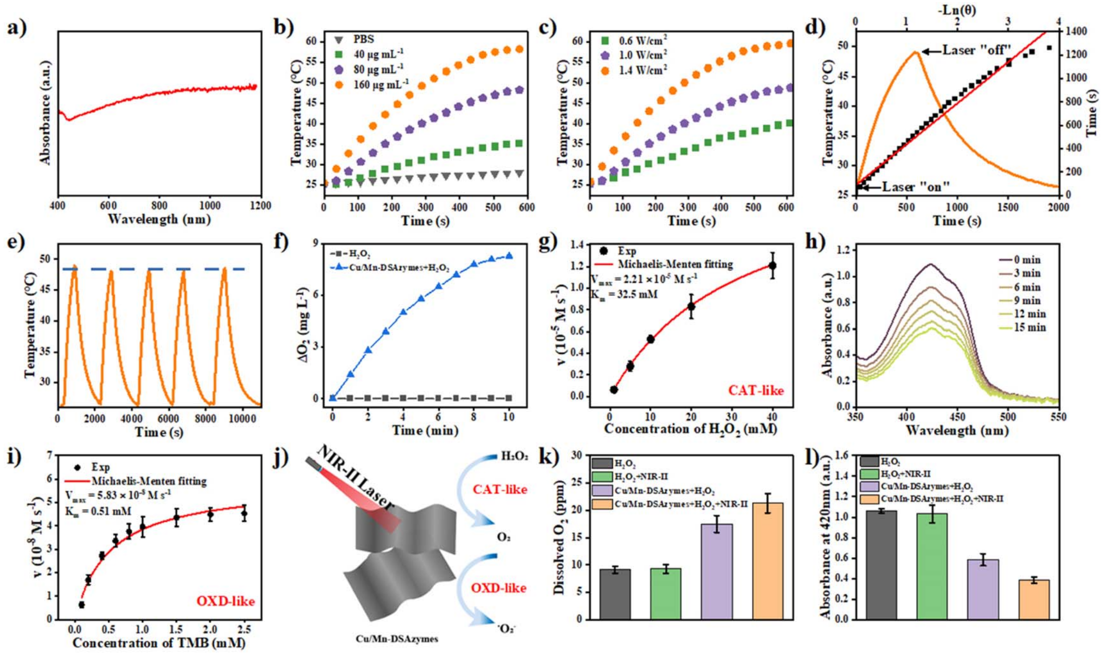

Fig. 2 (a) The UV-vis-NIR absorption spectra of Cu/Mn-DSAzymes. (b) Temperature elevation curve of Cu/Mn-DSAzymes at different concentrations (0, 40, 80, and 160 μg mL^{-1}) under an irradiation of 1064 nm laser (1 W cm^{-2}). (c) Temperature elevation curve of Cu/Mn-DSAzymes (80 μg mL^{-1}) under an irradiation of 1064 nm laser at different power intensities (0.6, 1.0, and 1.4 W cm^{-2}). (d) Calculation of the photothermal conversion efficiency at 1064 nm based on the heating and cooling curves of Cu/Mn-DSAzymes. (e) Alternate heating and cooling curves of Cu/Mn-DSAzymes (1064 nm, 1.0 W cm^{-2}). (f) O_2 generation from H_2O_2 decomposition through Cu/Mn-DSAzymes catalysis. (g) Michaelis–Menten kinetic analysis for the CAT-like action of Cu/Mn-DSAzymes with H_2O_2 as the substrate. (h) Depletion of DPBF owing to $^{\bullet}O_2^-$ production in the presence of Cu/Mn-DSAzymes and H_2O_2. (i) Michaelis–Menten kinetic analysis for the OXD-like activity of Cu/Mn-DSAzymes with TMB as the substrate. (j) Schematic diagram for the generation of O_2 and $^{\bullet}O_2^-$ by the Cu/Mn-DSAzymes-mediated CAT-like and OXD-like cascade reaction. (k) O_2 generation from H_2O_2 decomposition through Cu/Mn-DSAzymes catalysis with or without 1064 nm laser irradiation. (l) Depletion of DPBF for detecting the OXD-like activity of Cu/Mn-DSAzymes with or without 1064 nm laser irradiation.

the presence of H_2O_2, indicating that Cu/Mn-DSAzymes had good CAT-like properties. Moreover, during the CAT-like process, the Cu/Mn-DSAzymes possessed typical Michaelis–Menten kinetics, and their Michaelis–Menten constant (K_m) and maximal reaction velocity (V_{max}) were calculated as 32.5 mM and 2.21×10^{-5} Ms^{-1}, respectively (Fig. 2g). Therefore, through CAT-like catalysis, Cu/Mn-DSAzymes can efficiently mediate H_2O_2 decomposition into O_2 at the wound sites, and create the prerequisite for triggering OXD-like activity to generate $^{\bullet}O_2^-$ in a hypoxic tumor. The OXD-like activity of the Cu/Mn-DSAzymes was also evaluated using 1,3-diphenylisobenzonfuran (DPBF) as a probe. The absorbance of DPBF at 420 nm can be bleached by oxygen-containing radicals. As shown in Fig. 2h, the absorbance at 420 nm decreased remarkably after the addition of Cu/Mn-DSAzymes to the solution of DPBF and H_2O_2, confirming that Cu/Mn-DSAzymes had an obvious OXD-like activity to generate $^{\bullet}O_2^-$. Furthermore, when 3,3′,5,5′-tetramethylbenzidine (TMB) was used as the reaction substrate, the key kinetic parameters for OXD action, including K_m and V_{max} values, were 0.51 mM and 5.83×10^{-8} Ms^{-1}, respectively (Fig. 2i). Thus, Cu/Mn-DSAzymes possessed good dual CAT-like and OXD-like enzyme activities, and can efficiently catalyze the cascade enzymatic reactions (Fig. 2j and S2†). The Cu/Mn-DSAzymes converted H_2O_2 into O_2 by CAT-like catalysis, activating the catalytic activity of OXD, and then Cu/Mn-DSAzymes can continue to catalyze O_2 into $^{\bullet}O_2^-$. Moreover, the CAT-like and OXD-like activities of CNNs are negligible (Fig. S3 and S4†). It is worth noting that the Cu/Mn dual single-atom, as efficient catalytic active sites, synergistically catalyzed the aforementioned cascade reactions. On the one hand, the atomically dispersed Mn^{4+} sites on Cu/Mn-DSAzymes acted as highly active catalytic centers during the CAT-like process, effectively mediating H_2O_2 into O_2. On the other hand, the Cu^{+} single-atom sites anchored on Cu/Mn-DSAzymes possessed high OXD-like activity and efficiently catalyzed O_2 into $^{\bullet}O_2^-$. In addition, as shown in Fig. 2k and l, the CAT-like and OXD-like catalysis of Cu/Mn-DSAzymes can be further enhanced by their NIR-II-triggered photothermal effect. Collectively, these results demonstrated that Cu/Mn-DSAzymes can generate O_2 and $^{\bullet}O_2^-$ by CAT- and OXD-like catalysis, and possessed NIR-II-enhanced dual enzyme catalysis, showing great potential in bacteria-infected wound treatment.

To enhance the biocompatibility of Cu/Mn-DSAzymes, mPEG-COOH was modified onto their surface by electrostatic adherence. The resulting PEGylated Cu/Mn-DSAzymes showed a negative zeta potential value, suggesting successful modification (Fig. S5†). The resulting PEGylated Cu/Mn-DSAzymes can be stably dispersed in different physiological media (Fig. S6†), and no Cu or Mn leaching was found during incubation in physiological media (Fig. S7†). Therefore, these results indicated that PEGylated Cu/Mn-DSAzymes could be applied to *in vitro* and *in vivo* experiments. To simplify the expression, the PEGylated Cu/Mn-DSAzymes was subsequently abbreviated to Cu/Mn-DSAzymes.

3.3. *In vitro* antibacterial effect mediated by Cu/Mn-DSAzymes

Encouraged by their favorable NIR-II photothermal effect, as well as their excellent CAT-like and OXD-like activities, the *in vitro* antibacterial effect of Cu/Mn-DSAzymes was evaluated against both Gram-positive bacteria (*Escherichia coli*, *E. coli*) and multidrug-resistant pathogenic bacteria (methicillin-resistant *Staphylococcus aureus*, MRSA). The *E. coli* and MRSA bacteria were then separately treated with PBS + H_2O_2, NIR-II + H_2O_2, Cu/Mn-DSAzymes, Cu/Mn-DSAzymes + NIR-II, Cu/Mn-DSAzymes + H_2O_2, and Cu/Mn-DSAzymes + H_2O_2 + NIR-II groups. First, MRSA bacteria with different treatments were stained using 2′,7′-dichlorofluorescin diacetate (DCFH-DA) as the fluorescent probe for detecting the ROS (*i.e.*, $^{\bullet}O_2^{-}$) level (Fig. 3a). Compared to the PBS + H_2O_2, NIR-II + H_2O_2, Cu/Mn-DSAzymes, or Cu/Mn-DSAzymes + NIR-II groups, the significantly elevated ROS level occurred in the group treated with Cu/Mn-DSAzymes + H_2O_2, as revealed by the obvious green fluorescence. This was attributed to the Cu/Mn-DSAzymes with remarkable dual CAT-like and OXD-like enzyme activities being able to catalyze the cascade enzymatic reactions with a low level of H_2O_2 as the initial reactant to effectively increased O_2 levels and produce abundant $^{\bullet}O_2^{-}$. Moreover, when MRSA bacteria were treated with Cu/Mn-DSAzymes + H_2O_2 + NIR-II, the ROS level could be further boosted by NIR-II laser irradiation, attributed to the enhanced dual enzyme catalysis of Cu/Mn-DSAzymes by photothermal effect. Next, the antibacterial activity of Cu/Mn-DSAzymes was investigated using colony-forming units (CFUs) on agar plates (Fig. 3b–d). Obvious *E. coli* and MRSA colony formations were observed in the PBS + H_2O_2, NIR-II + H_2O_2, or Cu/Mn-DSAzymes treatment groups. Accordingly, these three treatment groups showed no significant effect on the survival rate of bacteria. By contrast, the colonies and the survival rates of *E. coli* and MRSA obviously decreased upon being treated with the Cu/Mn-DSAzymes + NIR-II or Cu/Mn-DSAzymes + H_2O_2 groups, resulting from the photothermal or nanocatalytic antibacterial effect mediated by Cu/Mn-DSAzymes. However, such bactericidal efficiency was not sufficient for real clinical antibacterial applications, as surviving bacteria would rapidly proliferate, leading to reinfection. Notably, the Cu/Mn-DSAzymes + H_2O_2 + NIR-II group displayed outstanding antibacterial capability against *E. coli* and MRSA. It can be observed that after treatment with the Cu/Mn-DSAzymes + H_2O_2 + NIR-II group, almost no colonies were formed on the agar plates, and the survival rate of bacteria was close to 0%. This meant that the synergistic mild photothermal/nanocatalytic-therapy achieved more efficient bacteria killing than only mild photothermal therapy or only nanocatalytic therapy. Such excellent bacteria killing efficiency

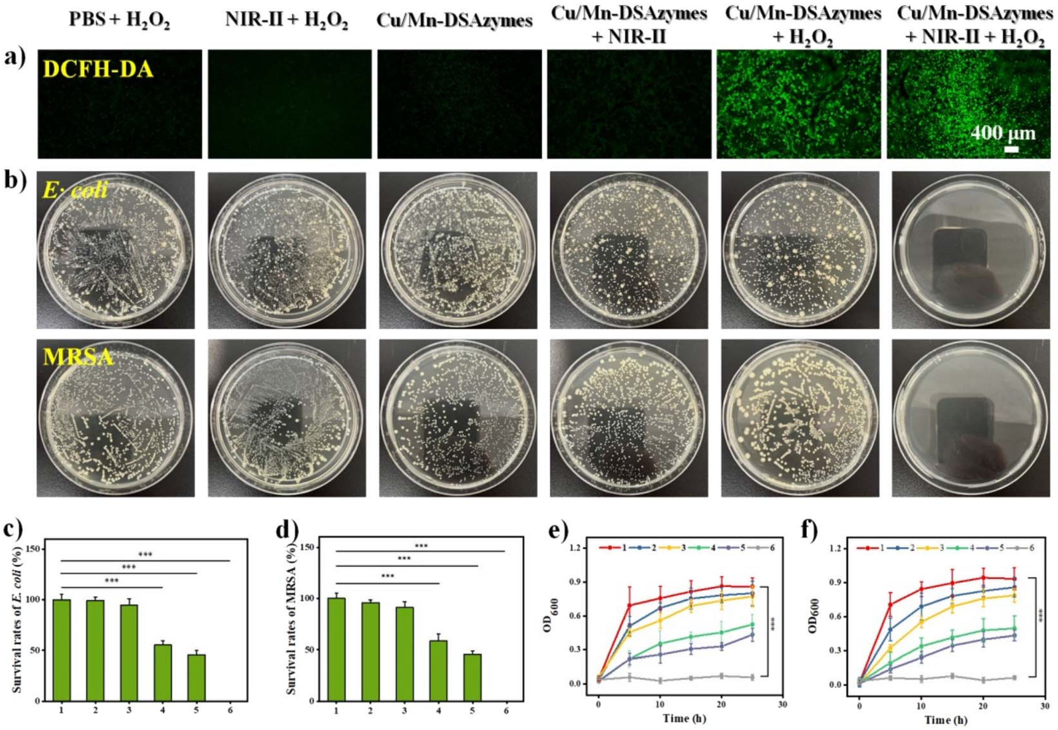

Fig. 3 (a) ROS (*i.e.*, $^{\bullet}O_2^{-}$) levels in MRSA were monitored by DCFH-DA after different treatments. (b) The pictures of *E. coli* and MRSA colonies on agar plates after different treatments. Corresponding survival rates of *E. coli* (c) and MRSA bacteria (d) after different treatments. The growth curve of *E. coli* (e) and MRSA bacteria (f) at OD 600 nm after different treatments. Group 1: PBS + H_2O_2; 2: NIR-II + H_2O_2; 3: Cu/Mn-DSAzymes; 4: Cu/Mn-DSAzymes + NIR-II; 5: Cu/Mn-DSAzymes + H_2O_2; 6: Cu/Mn-DSAzymes + H_2O_2 + NIR-II ($n = 3$, mean ± SD; ***$p < 0.001$, **$p < 0.01$ and *$p < 0.05$).

was likely attributed to the severe damage of the bacterial internal and external structures/properties, such as nucleic acids, proteins, and membrane permeability, caused by synergistic treatments.[9,34] Furthermore, these results were further confirmed by the bacteria growth curve (at OD 600 nm) upon different treatments (Fig. 3e and f).

Furthermore, the antibacterial mechanism of synergistic therapy was thoroughly investigated. The destruction of the bacterial membrane structure induced by ROS or photothermal effects could lead to bacterial killing.[9,10,35] First, the morphologies of *E. coli* and MRSA bacteria were observed by scanning electron microscopy (SEM) after different treatments (Fig. 4a). The bacteria treated with the PBS + H_2O_2, NIR-II + H_2O_2, or Cu/Mn-DSAzymes groups all showed smooth bacterial morphology and complete membrane structure. By contrast, after undergoing mild photothermal therapy or nanocatalytic therapy, the bacterial membrane morphology in the Cu/Mn-DSAzymes + NIR-II or Cu/Mn-DSAzymes + H_2O_2 groups displayed a certain degree of roughness, fragmentation, swelling, and collapse. These results suggested that the bacterial membrane could be partially destroyed by NIR-II-triggered photothermal effect or the dual enzyme activity-mediated $^{\bullet}O_2^-$. Notably, combining the photothermal effects and nanoenzyme properties of Cu/Mn-DSAzymes, the surface of the bacteria treated with the Cu/Mn-DSAzymes + H_2O_2 + NIR-II group showed severe dispersion, collapse, wrinkling, distortion, and even fracturing, indicating the significantly damaged bacteria membrane structure caused by synergistic therapy. Next, the double-staining of the fluorescent dye SYTO9 and propidium iodide (PI) on the bacteria was further performed to

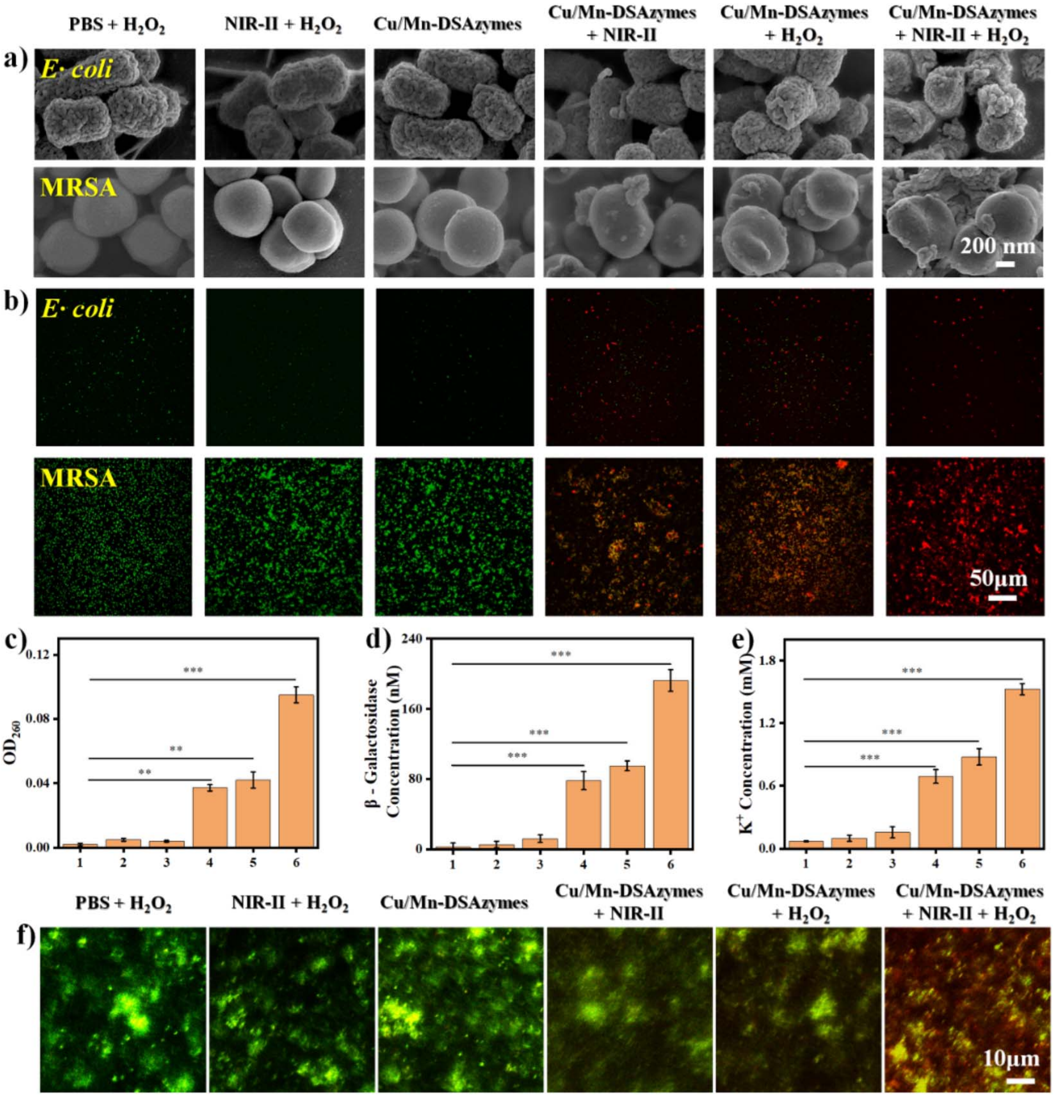

Fig. 4 (a) The SEM images of *E. coli* and MRSA after different treatments. (b) Live/dead staining images for *E. coli* and MRSA using confocal laser scanning microscopy after different treatments. The concentration of nucleic acids (c), β-galactosidase (d), and K^+ (e) in the culture medium of MRSA treated with different groups. (f) CLSM images of the live/dead staining assay of the MRSA biofilm treated with different groups. Group 1: PBS + H_2O_2; 2: NIR-II + H_2O_2; 3: Cu/Mn-DSAzymes; 4: Cu/Mn-DSAzymes + NIR-II; 5: Cu/Mn-DSAzymes + H_2O_2; 6: Cu/Mn-DSAzymes + H_2O_2 + NIR-II ($n = 3$, mean ± SD; $***p < 0.001$, $**p < 0.01$ and $*p < 0.05$).

determine the changes of the bacterial membrane structure upon different treatments. The green fluorescence indicated live bacteria and an intact bacterial membrane, while the red fluorescence represented dead bacteria and destruction of the bacterial membrane. As presented in Fig. 4b, the Cu/Mn-DSAzymes + NIR-II group led to some destruction of the bacterial membrane for *E. coli* and MRSA bacteria compared with the PBS + H_2O_2, NIR-II + H_2O_2, and Cu/Mn-DSAzymes groups, as revealed by the generation of evident red fluorescence signals. This was because the photothermal effect caused by the Cu/Mn-DSAzymes disrupted the bacterial membrane. The Cu/Mn-DSAzymes + H_2O_2 group also showed an obvious bacteria killing effect, originating from the abundant ROS triggered by the dual enzyme activities. Moreover, the strongest red fluorescence signals were observed from *E. coli* and MRSA bacteria treated with the Cu/Mn-DSAzymes + H_2O_2 + NIR-II group. This further confirmed that the bacterial membranes could be seriously destroyed by synergistic mild photothermal/nanocatalytic-therapy, thus endowing synergistic therapy with outstanding antibacterial effect. These imaging results of the live/dead staining bacteria were in agreement with the bacterial morphology alteration in SEM observation. Moreover, the disruption of the bacterial membrane can alter the membrane permeability, thereby further boosting bacterial killing. Thus, the permeability of MRSA bacterial membranes was evaluated upon different treatments (Fig. 4c–e). Compared to other treatment groups, MRSA bacteria treated with the Cu/Mn-DSAzymes + H_2O_2 + NIR-II group exhibited remarkable leakage of nucleic acids, β-galactosidase, and K^+. This indicated that the permeability of the MRSA bacterial membrane was significantly increased by Cu/Mn-DSAzymes-mediated synergistic therapy. Collectively, Cu/Mn-DSAzymes-mediated synergistic nanocatalytic and photothermal effects can result in high lethality to MRSA bacteria. This can be explained as follows: on the one hand, Cu/Mn-DSAzymes can efficiently catalyze the cascade enzymatic reactions with a low level of H_2O_2 as the initial reactant to produce lethal $^{\bullet}O_2^-$, severely damaging the membrane structure and altering the membrane permeability, which ultimately induced significant bacterial apoptosis; on the other hand, the photothermal effect triggered by Cu/Mn-DSAzymes can also induce bacterial apoptosis, and the photothermal effect can promote the cascade enzymatic reactions and increase the permeability of the bacterial membrane, thus enhancing $^{\bullet}O_2^-$ to destroy the membrane structure and accelerating bacterial apoptosis. In addition, the formation of biofilms was the main cause of resistance to anti-infectious therapy.[3] Therefore, the ability of synergistic therapy to resist the MRSA biofilm was investigated by plate culture assay. The presence of more dead biofilms directly corresponded to a darker red fluorescence color. As shown in Fig. 4f, after the MRSA biofilm was treated with the Cu/Mn-DSAzymes + H_2O_2 + NIR-II group, an intensive and strong red fluorescence caused by the death of the MRSA biofilm was observed, suggesting the efficient anti-biofilm ability of the Cu/Mn-DSAzymes-mediated synergistic therapy.

Next, the *in vitro* cytocompatibility of Cu/Mn-DSAzymes was investigated by cholecystokinin-8 (CCK-8) assay. The fibroblast L929 cells were first incubated with Cu/Mn-DSAzymes at different concentrations (0, 20, 40, 80, and 160 μg mL^{-1}) for 24 h to evaluate the cytotoxicity of Cu/Mn-DSAzymes. Cu/Mn-DSAzymes showed no significant effect on the survival rates of fibroblast L929 cells, even at the highest concentration of 160 μg mL^{-1}, suggesting that their cytotoxicity was extremely low (Fig. 5a). Furthermore, the L929 cells incubated with Cu/Mn-DSAzymes for 1, 3, or 5 days exhibited comparable cell viability with the PBS group, further demonstrating their good biocompatibility (Fig. 5b). In addition, the hemolysis ratio of Cu/Mn-DSAzymes at a concentration of up to extreme 4 mg mL^{-1} was only ∼13.5%, indicating that Cu/Mn-DSAzymes would not cause the rupture and lysis of red blood cells (RBCs) (Fig. 5c). O_2 release during treatment could enhance the activity of fibroblasts and mediate fibroblast chemotaxis towards the wound site, as well as promote collagen synthesis and angiogenesis, accelerating the wound healing and tissue regeneration.[36,37] An O_2 specific probe ([Ru(dpp)$_3$]Cl, RDPP) was used to confirm the intracellular oxygen level. As shown in Fig. 5d, a significant decrease in the red fluorescence of the RDPP probe was found in L929 cells treated with Cu/Mn-DSAzymes + H_2O_2. This was attributed to an obvious increase in the intracellular oxygen level caused by the CAT-like properties of Cu/Mn-DSAzymes. Moreover, when L929 cells were treated with Cu/Mn-DSAzymes + H_2O_2 + NIR-II, the intracellular oxygen level could be further boosted by NIR-II laser irradiation, resulting from the enhanced CAT-like catalysis of Cu/Mn-DSAzymes by photothermal effect. In addition, the effect of O_2 release mediated by Cu/Mn-DSAzymes on the L929 cell migration ability was evaluated by cell scratch assay and migration experiment (Fig. 5e). It was observed that the migration of L929 cells incubated with Cu/Mn-DSAzymes + H_2O_2 + NIR-II was obviously enhanced in comparison with cells incubated with other treatment groups. This implied that the Cu/Mn-DSAzymes-mediated O_2 release through synergistic CAT-like properties and photothermal effect contributed to the enhanced cell migration and proliferation. Thus, the Cu/Mn-DSAzymes-synergistic therapy not only had good biocompatibility, but also facilitated the cell proliferation and migration, benefiting the repair of damaged tissues.

3.4. *In vivo* antibacterial performance and wound healing mediated by Cu/Mn-DSAzymes

After validating the excellent antibacterial effect *in vitro*, a mouse model with a wound infected with MRSA was used to evaluate the *in vivo* synergetic antibacterial efficacy and wound healing ability mediated by Cu/Mn-DSAzymes. Firstly, the photothermal effect of Cu/Mn-DSAzymes on the mouse wound was evaluated. The *in vivo* thermal images (Fig. 6a) showed that the local wound temperature of the mouse treated with Cu/Mn-DSAzymes was increased to 49.5 °C within 10 min by adjusting the NIR-II laser power density to an appropriate level. This suggested a good photothermal effect *in vivo*, and offered a relatively safe and mild treatment temperature. Next, MRSA-infected full-thickness wounds were established on the back of mice, and MRSA infection was implemented.

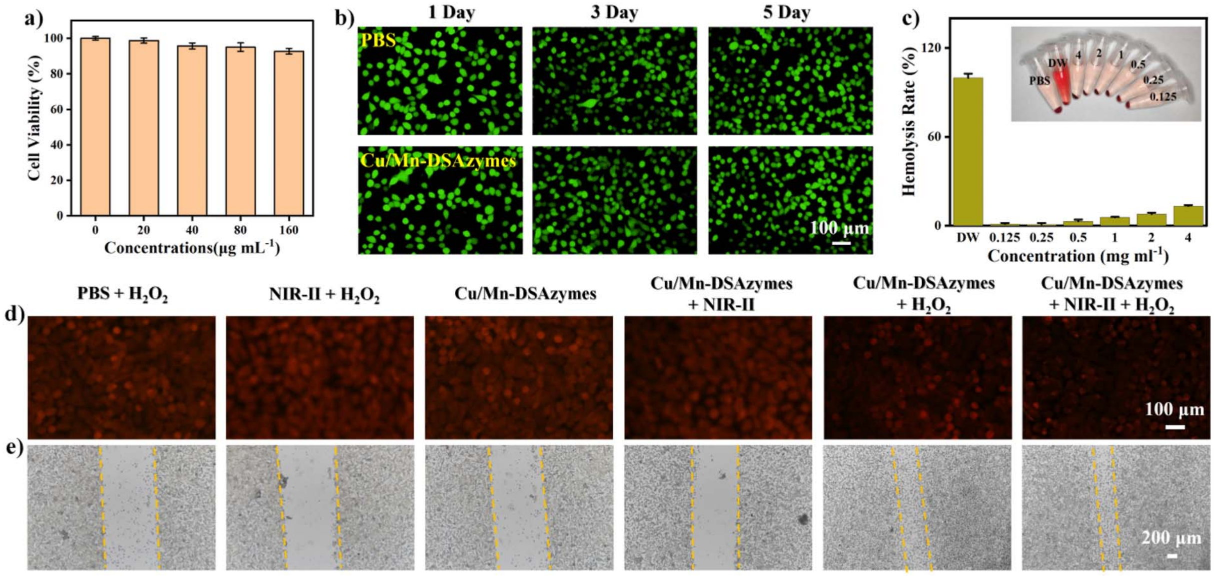

Fig. 5 (a) Viability of L929 fibroblast cells incubated with different concentrations of Cu/Mn-DSAzymes. (b) Fluorescence images for L929 fibroblast cells incubated with Cu/Mn-DSAzymes for 1, 3, and 5 days. Live/dead fibroblast L929 cells were green/red (calcein AM/PI). (c) Hemolysis ratio of Cu/Mn-DSAzymes. (d) Intracellular O_2 release detected by the RDPP probe after different treatments. (e) The migration of L929 fibroblast cells in the culture plate after different treatments.

Correspondingly, bacterial colonies could be clearly observed on agar plates cultured with MRSA collected from the infected wounds at day 1, indicating successful MRSA infection (Fig. S8†). The MRSA-infected wounds were then subjected to different treatments: PBS + H_2O_2, NIR-II + H_2O_2, Cu/Mn-DSAzymes, Cu/Mn-DSAzymes + NIR-II, Cu/Mn-DSAzymes + H_2O_2, and Cu/Mn-DSAzymes + H_2O_2 + NIR-II groups. The representative photographs of the wounds and the corresponding relative wound area at different time points are presented in Fig. 6b and c, respectively. The MRSA-infected wounds treated with PBS + H_2O_2, NIR-II + H_2O_2, or Cu/Mn-DSAzymes groups showed a very slow healing process with a wide wound area on day 9. This was due to the MRSA-infected wound possessing inferior self-healing capacity, which facilitated the degradation of collagen fibers and the accumulation of inflammatory cells, thereby resulting in tissue damage and hindered healing.[9,38] By contrast, the MRSA-infected wound displayed favorable tissue healing after being treated with the Cu/Mn-DSAzymes + NIR-II group. This was attributed to the fact that the photothermal therapy not only had an antibacterial effect, but also was beneficial to collagen synthesis, angiogenesis and accelerated blood circulation.[9,16,21] Moreover, the MRSA-infected wound treated with Cu/Mn-DSAzymes + H_2O_2 also exhibited improved tissue healing. This originated from the fact that the nanocatalytic therapy mediated by CAT- and OXD-like properties gave rise to a ROS-related antibacterial effect, as well as O_2-promoted cell proliferation, collagen synthesis, and angiogenesis effects.[36,37] Notably, compared with the above two single treatment groups and the other three control groups, the MRSA-infected wound treated with Cu/Mn-DSAzymes + H_2O_2 + NIR-II group had the least inflammation, the fastest healing rate, and the minimum wound area (6.6%), and the treated infected wound almost completely healed on day 9. Such superior antibacterial efficiency was due to the cooperative enhancement effects (*i.e.*, significant superadditive effects) caused by the Cu/Mn-DSAzymes-mediated synergistic mild photothermal/nanocatalytic-therapy. Particularly, such photothermal heating could promote a cascade CAT-like and OXD-like reaction to generate more O_2 and ROS, and could also increase the ROS permeability to the bacterial membrane, thereby boosting the antibacterial effect and facilitating tissue repair.[6,9,20] Meanwhile, the increased ROS at the wound sites likely disrupted the bacterial membrane to make it more susceptible to photothermal therapy, improving the mild photothermal antibacterial effectiveness.[16,25,26] Furthermore, to quantitatively evaluate the *in vivo* antibacterial ability of Cu/Mn-DSAzymes, bacteria samples collected from wound tissues on day 9 were incubated on agar plates (Fig. 6d). Compared to other groups, no evident colonies could be found in the Cu/Mn-DSAzymes + H_2O_2 + NIR-II group, further validating the excellent *in vivo* antibacterial ability. In addition, after treatment with the Cu/Mn-DSAzymes + H_2O_2 + NIR-II group, the hematoxylin and eosin (H&E) staining of mouse main organs (heart, liver, spleen, lung, and kidney) displayed no obvious histological abnormities and organ damage, demonstrating the negligible organ toxicity of Cu/Mn-DSAzymes (Fig. 6e). Moreover, the negligible changes in body weights of mice also indicated the good biocompatibility of Cu/Mn-DSAzymes (Fig. S9†). In short, the Cu/Mn-DSAzymes-mediated synergistic therapy was a versatile strategy to overcome MRSA bacterial infection and accelerate wound healing.

The histopathological analysis of the wound tissues after different treatments for 9 days was performed by hematoxylin and eosin (H&E) and Masson's trichrome staining, as well as

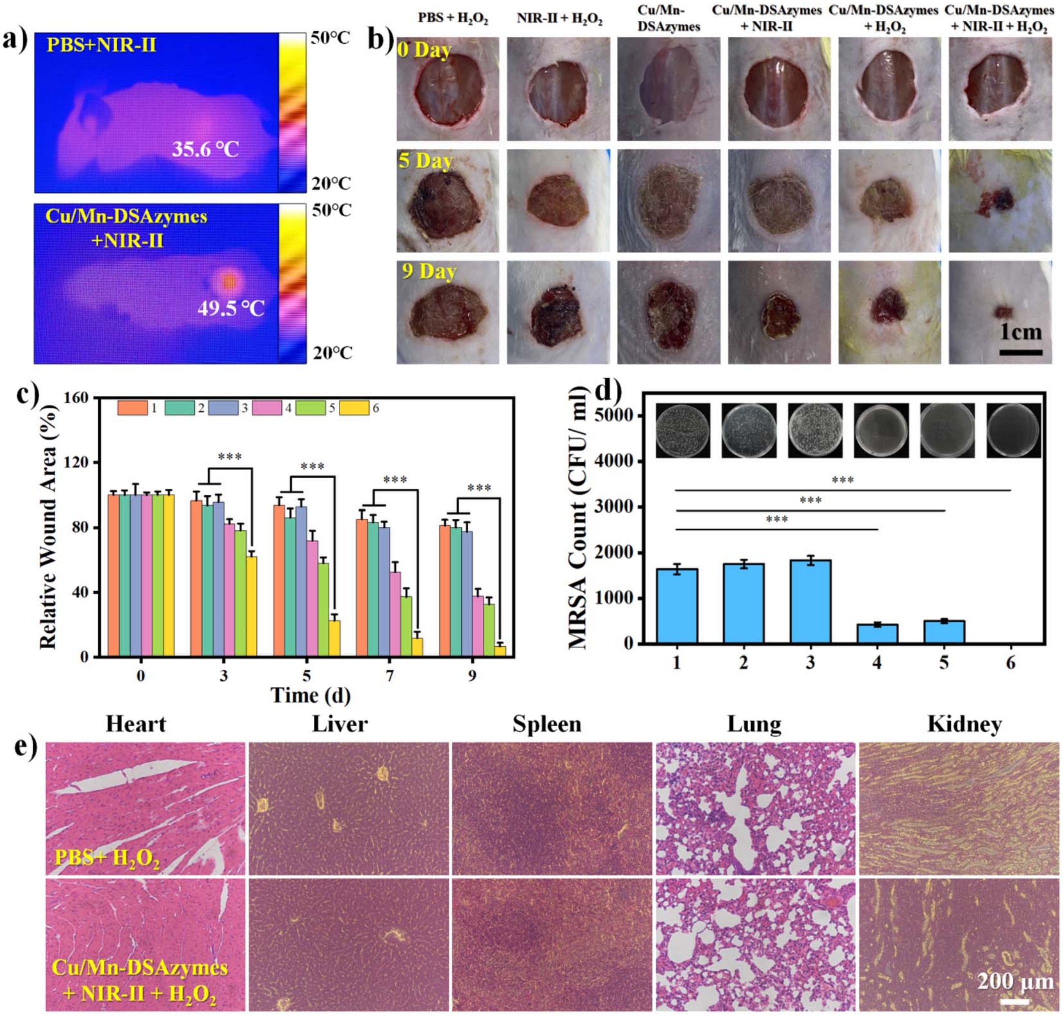

Fig. 6 (a) *In vivo* thermal images of the mice wound treated with PBS or Cu/Mn-DSAzymes upon 1064 nm laser irradiation for 10 min. (b) Photographs of the healing process of wounds infected with MRSA and treated with different groups. (c) Relative wound area of different treatment groups during 9 days. (d) Evaluation of bacterial colonies from the wound tissue with different treatments. Group 1: PBS + H_2O_2; 2: NIR-II + H_2O_2; 3: Cu/Mn-DSAzymes; 4: Cu/Mn-DSAzymes + NIR-II; 5: Cu/Mn-DSAzymes + H_2O_2; 6: Cu/Mn-DSAzymes + H_2O_2 + NIR-II. (e) H&E staining of the main organs upon treatment with PBS + H_2O_2 or Cu/Mn-DSAzymes + H_2O_2 + NIR-II ($n = 5$, mean ± SD; ***$p < 0.001$, **$p < 0.01$ and *$p < 0.05$).

CD86, CD206, and CD31 immunofluorescence staining. Infiltration of inflammatory cells into wounds and the resulting inflammatory response would significantly hinder tissue healing.[39,40] As shown in the H&E-stained sections (Fig. 7a), the wound tissue treated with the Cu/Mn-DSAzymes + H_2O_2 + NIR-II group showed no obvious inflammation, suggesting that the MRSA bacterial infection was effectively suppressed. Moreover, relatively intact epidermis and regenerated dermis appendages (including hair follicles and granulation) were observed in the Cu/Mn-DSAzymes + H_2O_2 + NIR-II group, indicating significant wound healing. In contrast, the other groups still had different levels of inflammation and fragmentary epidermal layers, suggesting that the inflamed tissues were not fully treated. The formation of collagen enabled cell migration and acted as a foundation for the extracellular matrix, which was vital for wound healing.[6,9] Masson staining was employed to assess collagen deposition during the wound healing progress (Fig. 7b). The wound tissues treated with the Cu/Mn-DSAzymes + H_2O_2 + NIR-II group presented abundant collagen with dense and organized structures, beneficial from the outstanding antibacterial and anti-infective efficacy of synergistic therapy. This verified that the Cu/Mn-DSAzymes-mediated synergistic mild photothermal/nanocatalytic-therapy can effectively accelerate tissue regeneration and promote wound healing. However, fewer collagen fibers with a loosely packed distribution were observed in the other groups, which could be due to tissue inflammation and residual bacteria. Moreover, the phenotype of the macrophages in the wound tissue was an important indicator of the inflammatory response.[39,40] Thus, the infiltration of macrophages at the wound sites (Fig. 7c, d, f and g) was further evaluated by immunofluorescence staining of CD86 (a typical surface marker for M1 macrophages) and CD206 (a typical surface marker for M2 macrophages). Compared to other groups, wound tissues treated with the Cu/Mn-DSAzymes

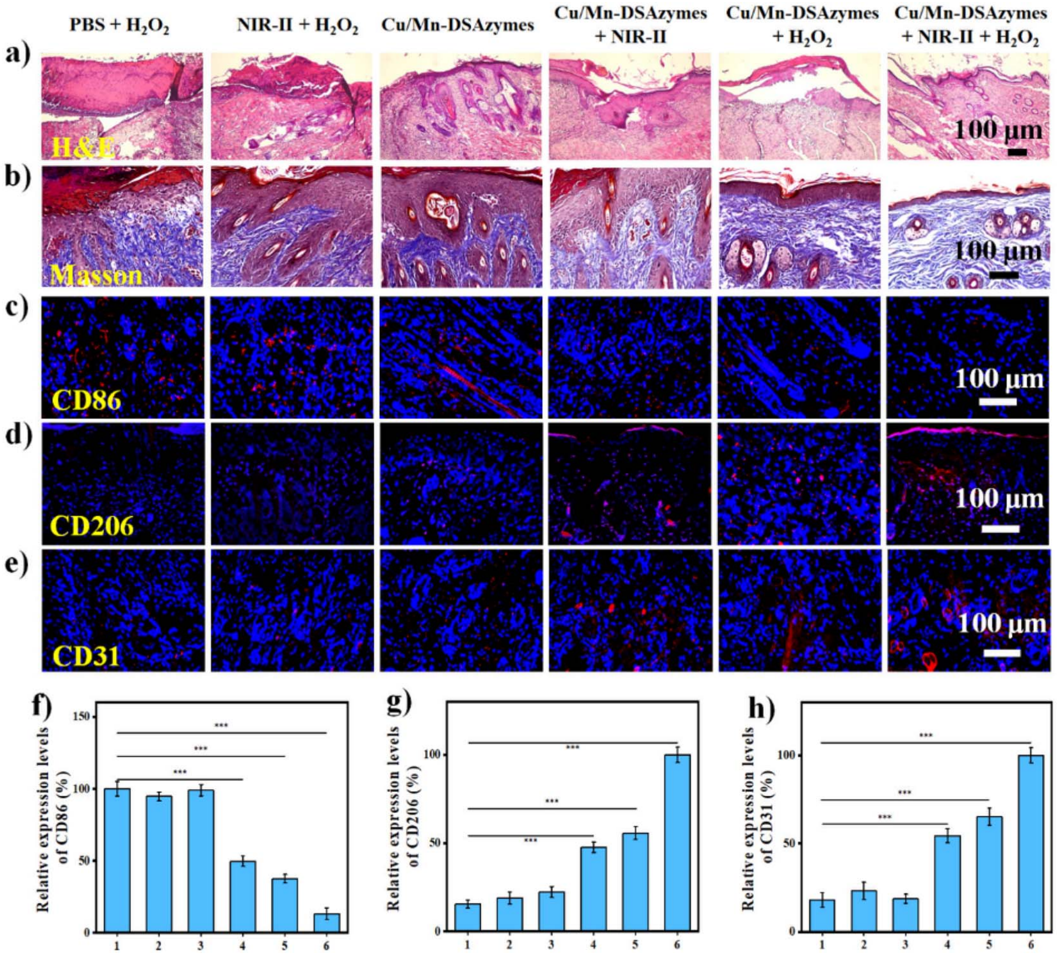

Fig. 7 (a) H&E staining of tissues at MRSA-infected wound sites on day 9 after different treatments. (b) Masson's trichrome staining of tissues at MRSA-infected wound sites on day 9 after different treatments. Immunofluorescence staining of (c) CD86 for identifying M1 phenotype macrophages and (d) CD206 for identifying M2 phenotype macrophages in MRSA-infected wounds treated with different groups at day 9. Macrophages were stained with CD86 or CD206 in red, and the nuclei were stained with DAPI in blue. (e) Immunofluorescence staining of CD31 for identifying angiogenesis in MRSA-infected wound tissues after 9 days of treatment. Neovascularization was stained with CD31 in green, and the nuclei were stained with DAPI in blue. Relative expression levels of (f) CD86, (g) CD206, and (h) CD31, based on immunofluorescence staining for (c) CD86 of M1 phenotype macrophages, (d) CD206 of M2 phenotype macrophages, and (e) CD31 of neovascularization in MRSA-infected wound tissues after 9 days of treatment, respectively. Group 1: PBS + H_2O_2; 2: NIR-II + H_2O_2; 3: Cu/Mn-DSAzymes; 4: Cu/Mn-DSAzymes + NIR-II; 5: Cu/Mn-DSAzymes + H_2O_2; 6: Cu/Mn-DSAzymes + H_2O_2 + NIR-II ($n = 5$, mean ± SD; $***p < 0.001$, $**p < 0.01$ and $*p < 0.05$).

+ H_2O_2 + NIR-II group displayed markedly reduced CD86-positive M1 macrophages that facilitated inflammation, whereas there was a significant increase in the CD206-positive M2 macrophages that restrained inflammation and boosted tissue repair. The results suggested that the Cu/Mn-DSAzymes-mediated synergistic therapy can effectively alleviate the inflammatory response, and promote the establishment of a microenvironment conducive to wound repair. In addition, angiogenesis was an essential factor in wound healing, which would supply sufficient nutrients and oxygen to promote tissue recovery.[6,16,38] CD31, a representative biomarker associated with the formation of blood vessels and the level of angiogenesis, was then evaluated by immunofluorescence staining (Fig. 7e and h). Compared with other groups, significant expression of CD31, marked by red fluorescence, was found in the Cu/Mn-DSAzymes + H_2O_2 + NIR-II group, indicating greatly enhanced proangiogenic effect. This was likely attributed to the following reasons: on the one hand, the combined photothermal effect and O_2 release during tissue repair could boost blood circulation and vascular regeneration. On the other hand, the strong antibacterial ability caused by the synergistic photothermal effect and ROS significantly inhibited the inflammatory response and accelerated wound healing. Overall, these results indicated that the Cu/Mn-DSAzymes-mediated synergistic mild photothermal/nanocatalytic-therapy possessed dramatic antibacterial effects against MDR bacteria and significantly reduced the inflammation at the wound site. Moreover, the combined photothermal effect and O_2 release induced by the synergistic therapy promoted macrophage polarization to reparative M2 phenotype, collagen deposition, and angiogenesis, considerably accelerating tissue regeneration and wound healing.

4 Conclusions

In summary, we developed a multifunctional Cu/Mn dual single-atom nanozyme (Cu/Mn-DSAzymes)-based synergistic mild photothermal/nanocatalytic-therapy for MDR bacteria-infected wounds. Cu/Mn-DSAzymes with collaborative effects exhibit remarkable dual CAT-like and OXD-like enzyme activities, and can efficiently catalyze the cascade enzymatic reactions with a low level of H_2O_2 as the initial reactant to produce reparative O_2 and lethal $^{\bullet}O_2^-$. Moreover, the black N-doped carbon nanosheet supports of Cu/Mn-DSAzymes show superior NIR-II-triggered photothermal performance, endowing them with photothermal-enhanced dual enzyme catalysis. In addition, such enhanced dual enzyme catalysis likely improves the susceptibility and lethality of photothermal effects on MDR bacteria. *In vitro* and *in vivo* studies demonstrate that Cu/Mn-DSAzymes-mediated synergistic nanocatalytic and photothermal effects possess dramatic antibacterial outcomes against MDR bacteria, and obviously reduced the inflammation at the wound sites. Moreover, the combined photothermal effect and O_2 release mediated by Cu/Mn-DSAzymes promotes macrophage polarization to reparative M2 phenotype, collagen deposition, and angiogenesis, considerably accelerating wound healing. Therefore, the Cu/Mn-DSAzyme-based synergetic dual-modal antibacterial therapy is a promising strategy for MDR bacteria-infected wound treatment, owing to their excellent antibacterial ability and significant tissue remodeling effects.

Conflicts of interest

The authors declare no conflict of interest.

Acknowledgements

The authors are grateful to the R&D Program of Beijing Municipal Education Commission (KZ202210011015). The authors are thankful for the support of the BSRF (Beijing Synchrotron Radiation Facility) during the XAFS measurements.

References

1 L. Rizzello and P. P. Pompa, *Chem. Soc. Rev.*, 2014, **43**, 1501–1518.

2 P. P. Kalelkar, M. Riddick and A. J. García, *Nat. Rev. Mater.*, 2022, **7**, 39–54.

3 Y. Zhang, D. Li, J. Tan, Z. Chang, X. Liu, W. Ma and Y. Xu, *Small*, 2021, **17**, 2005739.

4 W. Jia, H. Li, L. Zhao and J. K. Nicholson, *Nat. Rev. Drug Discovery*, 2008, **7**, 123–129.

5 Q. Xu, X. Li, Y. Jin, L. Sun, X. Ding, L. Liang, L. Wang, K. Nan, J. Ji and H. Chen, *Nanoscale*, 2017, **9**, 19245–19254.

6 X. Fan, X. Wu, F. Yang, L. Wang, K. Ludwig, L. Ma, A. Trampuz, C. Cheng and R. Haag, *Angew. Chem.*, 2022, **134**, e202113833.

7 Z. Yuan, C. Lin, Y. He, B. Tao, M. Chen, J. Zhang, P. Liu and K. Cai, *ACS Nano*, 2020, **14**, 3546–3562.

8 Y. Li, X. Liu, Z. Cui, Y. Zheng, H. Jiang, Y. Zhang, Y. Liang, Z. Li, S. Zhu and S. Wu, *ACS Nano*, 2022, **16**, 14860–14873.

9 S. Cheng, M. Qi, W. Li, W. Sun, M. Li, J. Lin, X. Bai, Y. Sun, B. Dong and L. Wang, *Adv. Healthcare Mater.*, 2023, **12**, 2202652.

10 K. Wu, D. Zhu, X. Dai, W. Wang, X. Zhong, Z. Fang, C. Peng, X. Wei, H. Qian, X. Chen, X. Wang, Z. Zha and L. Cheng, *Nano Today*, 2022, **43**, 101380.

11 L. Li, S. Cao, Z. Wu, R. Guo, L. Xie, L. Wang, Y. Tang, Q. Li, X. Luo, L. Ma, C. Cheng and L. Qiu, *Adv. Mater.*, 2022, **34**, 2108646.

12 Y. Ai, Z. N. Hu, X. Liang, H. b. Sun, H. Xin and Q. Liang, *Adv. Funct. Mater.*, 2021, **32**, 2110432.

13 Y. Yang, X. Wu, L. Ma, C. He, S. Cao, Y. Long, J. Huang, R. D. Rodriguez, C. Cheng and C. Zhao, *Adv. Mater.*, 2021, **33**, 2005477.

14 L. Ma, F. Jiang, X. Fan, L. Wang, C. He, M. Zhou, S. Li, H. Luo, C. Cheng and L. Qiu, *Adv. Mater.*, 2020, **32**, 2003065.

15 L. Li, L. Cao, X. Xiang, X. Wu, M. Lang, F. Chen, S. Cao, C. Cheng, D. Deng and L. Qiu, *Adv. Funct. Mater.*, 2021, **31**, 2107530.

16 P. Zhao, Y. Zhang, X. Chen, C. Xu, J. Guo, M. Deng, X. Qu, P. Huang, Z. Feng and J. Zhang, *Adv. Sci.*, 2023, **10**, 2206585.

17 Y. Wu, Q. Liao, L. Wu, Y. Luo, W. Zhang, M. Guan, H. Pan, L. Tong, P. K. Chu and H. Wang, *ACS Nano*, 2021, **15**, 17854.

18 X. Zhang, J. F. Du, Z. Guo, J. Yu, Q. Gao, W. Y. Yin, S. Zhu, Z. J. Gu and Y. L. Zhao, *Adv. Sci.*, 2019, **6**, 1801122.

19 Y. Wang, W. Niu, X. Qu and B. Lei, *ACS Appl. Mater. Interfaces*, 2022, **14**, 4946.

20 Z. Zhou, Y. Wang, F. Peng, F. Meng, J. Zha, L. Ma, Y. Du, N. Peng, L. Ma, Q. Zhang, L. Gu, W. Yin, Z. Gu and C. Tan, *Angew. Chem., Int. Ed.*, 2022, **61**, e20115939.

21 Z. Guo, Z. Zhang, N. Zhang, W. Gao, J. Li, Y. Pu, B. He and J. Xie, *Bioact. Mater.*, 2022, **15**, 203–213.

22 D. Peng, G. Liu, Y. He, P. Gao, S. Gou, J. Wu, J. Yu, P. Liu and K. Cai, *Biomater. Sci.*, 2021, **9**, 7483.

23 C. Liu, S. Li, R. Ma, C. Ji, K. Müllen and M. Yin, *Nano Today*, 2022, **42**, 101363.

24 G. Ma, Z. Liu, C. Zhu, H. Chen, R. T. Kwok, P. Zhang, B. Z. Tang, L. Cai and P. Gong, *Angew. Chem., Int. Ed.*, 2022, **61**, e202207213.

25 M. Chang, Z. Hou, M. Wang, D. Wen, C. Li, Y. Liu, Y. Zhao and J. Lin, *Angew. Chem., Int. Ed.*, 2022, **61**, e202209245.

26 M. Chang, Z. Hou, M. Wang, C. Yang, R. Wang, F. Li, D. Liu, T. Peng, C. Li and J. Lin, *Angew. Chem., Int. Ed.*, 2021, **60**, 12971–12979.

27 M. Huo, L. Wang, H. Zhang, L. Zhang, Y. Chen and J. Shi, *Small*, 2019, **15**, 1901834.

28 L. Wang, Q. Yang, M. Huo, D. Lu, Y. Gao, Y. Chen and H. Xu, *Adv. Mater.*, 2021, **33**, 2100150.

29 Y. He, X. Yang, Y. Li, L. Liu, S. Guo, C. Shu, F. Liu, Y. Liu, Q. Tan and G. Wu, *ACS Catal.*, 2022, **12**, 1216–1227.

30 W. Zhu, L. Zhang, S. Liu, A. Li, X. Yuan, C. Hu, G. Zhang, W. Deng, K. Zang and J. Luo, *Angew. Chem., Int. Ed.*, 2020, **59**, 12664–12668.

31 J. Xu, X. Zheng, Z. Feng, Z. Lu, Z. Zhang, W. Huang, Y. Li, D. Vuckovic, Y. Li, S. Dai, G. Chen, K. Wang, H. Wang,

J. K. Chen, W. Mitch and Y. Cui, *Nat. Sustainability*, 2020, **4**, 233–241.

32 D. R. Baer, D. L. Blanchard, M. H. Engelhard and J. M. Zachara, *Surf. Interface Anal.*, 1991, **17**, 25–30.

33 Y. Zhang, Q. Shen, Q. Li, P. He, J. Li, F. Huang, J. Wang, Y. Duan, C. Shen, F. Saleem, Z. Luo and L. Wang, *Adv. Sci.*, 2021, **8**, 2100386.

34 Z. Chen, S. Zheng, Z. Shen, J. Cheng, S. Xiao, G. Zhang, S. Liu and J. Hu, *Angew. Chem., Int. Ed.*, 2022, **61**, e202204526.

35 W. Wang, F. Wu, Q. Zhang, N. Zhou, M. Zhang, T. Zheng, Y. Li and B. Z. Tang, *ACS Nano*, 2022, **16**, 7961–7970.

36 Y. Liang, J. He and B. Guo, *ACS Nano*, 2021, **15**, 12687.

37 Y. Guan, H. Niu, Z. Liu, Y. Dang, J. Shen, M. Zayed, L. Ma and J. Guan, *Sci. Adv.*, 2021, **7**, eabj0153.

38 D. R. Osmon, E. F. Berbari, A. R. Berendt, D. Lew, W. Zimmerli, J. M. Steckelberg, N. Rao, A. Hanssen and W. R. Wilson, *Clin. Infect. Dis.*, 2013, **56**, 1–10.

39 W. Liu, R. Gao, C. Yang, Z. Feng, W. Ou-Yang, X. Pan, P. Huang, C. Zhang, D. Kong and W. Wang, *Sci. Adv.*, 2022, **8**, eabn7006.

40 C. Tu, H. Lu, T. Zhou, W. Zhang, L. Deng, W. Cao, Z. Yang, Z. Wang, X. Wu and J. Ding, *Biomaterials*, 2022, **286**, 121597.